J. Fluid Mech. (2010), *vol.* 648, *pp.* 381–404.
doi:10.1017/S0022112009993181

On the role of the ambient fluid on gravitational granular flow dynamics

C. MERUANE[1,2]†, A. TAMBURRINO[1] AND O. ROCHE[2]

[1]Departamento de Ingeniería Civil, Universidad de Chile, Blanco Encalada 2002, Casilla 228-3, Santiago, Chile

[2]Laboratoire Magmas et Volcans, UMR Unversité Blaise Pascal-CNRS-IRD, 5 rue Kessler, 63038 Clermont-Ferrand, France

(Received 3 June 2009; revised 29 October 2009; accepted 29 October 2009)

The effects of the ambient fluid on granular flow dynamics are poorly understood and commonly ignored in analyses. In this article, we characterize and quantify these effects by combining theoretical and experimental analyses. Starting with the mixture theory, we derive a set of two-phase continuum equations for studying a compressible granular flow composed of homogenous solid particles and a Newtonian ambient fluid. The role of the ambient fluid is then investigated by studying the collapse and spreading of two-dimensional granular columns in air or water, for different solid particle sizes and column aspect (height to length) ratios, in which the front speed is used to describe the flow. The combined analysis of experimental measurements and numerical solutions shows that the dynamics of the solid phase cannot be explained if the hydrodynamic fluid pressure and the drag interactions are not included in the analysis. For instance, hydrodynamic fluid pressure can hold the reduced weight of the solids, thus inducing a transition from dense-compacted to dense-suspended granular flows, whereas drag forces counteract the solids movement, especially within the near-wall viscous layer. We conclude that in order to obtain a realistic representation of gravitational granular flow dynamics, the ambient fluid cannot be neglected.

1. Introduction

Gravitational granular flows are common in nature. Typical geophysical examples include debris avalanches, pyroclastic flows, landslides, cliff collapses and submarine avalanches. As the dynamics of these flows involve different aspects of fluid mechanics, plasticity theory, solid mechanics and rheology (Wang & Hutter 2001), the combination of experimental and theoretical studies, as well as field observations and numerical simulations, is often required for their understanding (Ancey 2007). Although in specific cases our knowledge of the dynamics of granular flows has greatly improved (Goldhirsch 2003), so far no widely accepted set of governing equations exists.

A granular flow can be studied by considering the particular dynamics of at least two constituents: the ambient viscous fluid and the solid phase. Therefore, in order to describe the dynamics of the solid phase, the role of the ambient fluid should be

† Email address for correspondence: cmeruane@ing.uchile.cl

taken into account (Iverson 1997; Iverson & Denlinger 2001). In spite of this, one of the first works considering the interstitial fluid dynamics is the recent two-fluid model of Pitman & Le (2005), which is based on the early studies of Anderson & Jackson (1967). In fact, most studies on granular flows commonly ignore the presence of the fluid phase (e.g. Hutter, Wang & Pudasaini 2005; Campbell 2006). This is justified by the facts (i) that the solid particles are much denser than the ambient fluid, so that the analysis is based only on interactions among particles (Campbell 1990; Goldhirsch 2003); or (ii) that the bulk density of the solid phase remains constant during rapid granular motion, thus neglecting the compressible nature of the granular flows because of dilatation and compaction of the flow during acceleration and deceleration stages, respectively (Hutter *et al.* 2005).

The role of the ambient fluid can be investigated through a two-phase continuum model, considering the respective relationships that describe the interactions between the constituents (Drew 1983). Two different continuum theories can be followed: the mixture theory (Truesdell 1957) and the phase-averaged theory (Anderson & Jackson 1967). The mixture theory was formulated for studying the dynamics of mixtures of gases, through a generalization of basis and principles of continuous mechanics. The key abstraction in this theory is that, at any time, every point in space is occupied simultaneously by one particle of each constituent (Truesdell 1984). In order to derive a similar approach for fluid–solid mixtures, immiscibility of the constituents was considered by introducing the volume fraction of the components as additional kinematic variables (e.g. Bedford 1983; Passman, Nunziato & Walsh 1984). On the other hand, the phase-averaged formulation is based on an average of the mass and momentum balance laws for fluid and solid constituents over time or volume (Anderson & Jackson 1967; Drew 1983). Even if both theories allow the study of the dynamics of fluid–solid mixtures, they give different representations of the constitutive relations (Joseph & Lundgren 1990). A major challenge is to unify both theories and obtain a unique set of governing equations.

The purpose of the present paper is to improve the understanding of the role of the ambient viscous fluid on the dynamics of gravitational granular flows. In this context, we propose and validate a set of two-phase continuum equations for studying a granular flow composed of homogenous solid particles and a Newtonian ambient fluid. These governing equations are derived based on fundamental principles of the mixture theory and have two important characteristics: they consider the compressible nature of a granular flow and they are able to dynamically create interfaces. With this set of governing equations, the role of the ambient viscous fluid on the dynamics of gravitational granular flows is analysed experimentally and numerically for the collapse and spreading of a two-dimensional granular column in air or water, for different solid particle sizes and column aspect (height to length) ratios. We have chosen this particular configuration because it has widely been studied, it is characterized by an unsteady behaviour with a transition between static and flowing states and it represents an ideal case to validate the non-hydrostatic model (e.g. Balmforth & Kerswell 2005; Lajeunesse, Monnier & Homsy 2005; Lube *et al.* 2005; Staron & Hinch 2005; Larrieu, Staron & Hinch 2006).

This article is organized as follows. In § 2, the derivation of the governing equations is detailed. The experimental and numerical methods for the collapse and spreading of a two-dimensional granular column are described in § 3. The results are presented in § 4, in which we show that the ambient fluid modifies the granular flow dynamics via hydrodynamic fluid pressure and drag interactions. Finally, in § 5 we discuss the

results and show that in order to obtain a realistic representation of granular flow dynamics, the ambient fluid cannot be neglected.

2. Governing equations

2.1. *Mixture theory framework*

The mixture theory framework formulated for constituents with microstructure (Truesdell 1984) is used here to obtain the two-phase governing equations for a gravitational granular flow consisting of homogenous solid particles and a Newtonian ambient fluid.

Starting with this approach, we consider a fluid–solid mixture with both phases described as a continuum; that is, it is assumed that all the space x_i is filled simultaneously by particles of each phase at any time t. In order to identify the components of the mixture, the sub-index $n = s, f$ is used for solid and fluid phases, respectively. The mixture occupies a reference volume V, large compared with the particle size, and the phase n occupies a volume V_n within V, such as $V = V_s + V_f$. Each phase has a material density γ_n, a velocity u_{ni} and a volumetric concentration c_n. The partial density is defined as $\rho_n \equiv c_n \gamma_n$.

Because there is no mass transfer between phases, the mass and momentum conservation equations for each phase are written as (Truesdell 1984)

$$\frac{\partial \rho_n}{\partial t} + \frac{\partial (\rho_n u_{ni})}{\partial x_i} = 0, \tag{2.1}$$

$$\frac{\partial \rho_n u_{ni}}{\partial t} + \frac{\partial (\rho_n u_{nj} u_{ni})}{\partial x_j} = \rho_n f_{ni} + \frac{\partial T_{nij}}{\partial x_j} + \hat{m}_{ni}, \tag{2.2}$$

where f_{ni} represents the body forces acting on the phase n in the ith direction, T_{nij} denotes the partial stress tensor of the phase n and $\hat{m}_{ni}$ represents the reciprocal forces between the phases in the ith direction, such as $\hat{m}_{si} = -\hat{m}_{fi}$.

Constitutive relations for the interaction forces between the phases, as well as the stress tensor for each phase, are required to close the mathematical system of equations formed by (2.1) and (2.2), as discussed below.

2.2. *Constitutive relation for the interaction force*

As the constituents of a fluid–solid mixture remain physically separated in the space, the interaction force between the constituents is identified as superficial forces acting on a singular surface that separates the phases (Bedford 1983; Drew 1983; Morland & Sellers 2001). In order to obtain the mathematical representation of the constitutive equation from the integral balance laws of momentum, we identify this singular surface as the border ∂V_s of V_s on which a tensor of interaction surface forces $\hat{T}_{sij} = -\hat{T}_{fij}$ acts. Considering this, the integral balance laws of momentum for the case of solid particles in a gravitational field are expressed as

$$\int_V \left\{ \frac{\partial \rho_s u_{si}}{\partial t} + \frac{\partial (\rho_s u_{sj} u_{si})}{\partial x_j} \right\} \mathrm{d}V = \int_V \left\{ \rho_s g_i + \frac{\partial T_{sij}}{\partial x_j} \right\} \mathrm{d}V + \int_{\partial V_s} \hat{T}_{sij} n_j \, \mathrm{d}S. \tag{2.3}$$

Applying the divergence theorem on the last term of (2.3), and since $\mathrm{d}V_s = c_s \mathrm{d}V$, then

$$\int_{\partial V_s} \hat{T}_{sij} n_j \, \mathrm{d}S = \int_{V_s} \frac{\partial \hat{T}_{sij}}{\partial x_j} \, \mathrm{d}V_s = \int_V c_s \frac{\partial \hat{T}_{sij}}{\partial x_j} \, \mathrm{d}V. \tag{2.4}$$

Defining $\hat{T}_{sij}$ as the sum of a compression part $-\hat{p}_s\delta_{ij}$ and a shear stress part $\hat{\tau}_{sij}$, so

$$\hat{T}_{sij} = -\hat{p}_s\delta_{ij} + \hat{\tau}_{sij}, \tag{2.5}$$

where δ_{ij} denotes the delta Kronecker function, (2.3) is then written as

$$\frac{\partial \rho_s u_{si}}{\partial t} + \frac{\partial(\rho_s u_{sj} u_{si})}{\partial x_j} = \rho_s g_i + \frac{\partial T_{sij}}{\partial x_j} - c_s \frac{\partial \hat{p}_s}{\partial x_i} + c_s \frac{\partial \hat{\tau}_{sij}}{\partial x_j}. \tag{2.6}$$

Hence, the interaction force between the fluid and the solids in the momentum equations (2.2) is identified as

$$\hat{m}_{si} = -\hat{m}_{fi} = -c_s \frac{\partial \hat{p}_s}{\partial x_i} + c_s \frac{\partial \hat{\tau}_{sij}}{\partial x_j}. \tag{2.7}$$

The normal stress component in (2.7), $\hat{p}_s$, arises from the saturation constraint, that is, $c_s + c_f = 1$, and it specifies how one phase transmits forces to another keeping the contact between the phases (Passman *et al.* 1984). Although this surface pressure was identified in early studies on two-phase flows (Bedford 1983), so far no agreement exists on the specific form of this part of the constitutive equation (Joseph & Lundgren 1990). Most works have considered an equal pressure for all phases and then for the interface pressure (e.g. Drew 1983; Morland 1992), but later investigations have shown that this assumption is not physically possible (e.g. Jackson 2000; Morland & Sellers 2001). For instance, equal pressure assumption forces to define the partial pressure of each phase as $p_n = c_n p$, where $p = p_s + p_f$ is the pressure of the mixture. Under these circumstances, unphysical forces arise in the fluid phase given by volume concentration gradients, particularly under rest conditions, and an extra term, $p\partial_{x_i} c_f$, has to be included in order to obtain the correct force balance. We will analyse two simple cases in order to postulate that the interface pressure is the pressure of the fluid phase, and the correct mathematical representation for this interaction is presented in (2.7).

Let us consider first the static situation of a reservoir filled by solid particles with an interstitial fluid. The reduced weight of the solid particles is sustained by direct contacts among particles, identified here as the solid pressure p_s, and at places where no direct contact occurs the normal stress is the pressure of the surrounding fluid p_f. That is, the pressure of the fluid is sustained by both fluid and solid phases, while the reduced weight of the solids is sustained only by direct contacts among solid particles. Therefore, and in agreement with the Archimedes' principle, the interstitial fluid force balance is described between the equivalent weight of the fluid over the total mixture volume and the fluid pressure gradient, i.e. $\partial_{x_i} p_f = \gamma_f g$. Second, let us consider the dynamic case of solid particles falling down within a wide reservoir filled with a fluid, for instance water. We conducted laboratory tests by measuring the weight of such reservoir on a weigh scale and these revealed that while the particles were falling down, without touching the walls of the reservoir, the scale recorded the equivalent weight of water occupying the total volume of mixture, i.e. $\gamma_f(V_f + V_s)g$, and only once the particles impacted the bottom of the reservoir, the balance recorded the total weight of the fluid–particles system, i.e. $(\gamma_f V_f + \gamma_s V_s)g$. This second experiment shows the same fact described for the static case, that is, the reduced weight of the solid particles is not transmitted through the ambient fluid, so that different measurements will be recorded in the weigh scale depending on whether the particles are falling down or are resting on the bottom. These two simple analyses allow us to postulate that the interface pressure in (2.7) is the pressure of the fluid phase, p_f, i.e. $\hat{p}_s = p_f$.

Thus, the normal interaction force is $-c_s \partial_{x_i} p_f$, which can be identified as a buoyancy force, that is, it is the surface pressure exerted across the surface of the solids because of the surrounding fluid.

The last term of (2.7) arises from the stresses induced by the fluid when it passes through the interstices between the particles (e.g. Anderson & Jackson 1967). These stresses are well identified considering the fluidization of a bed of particles at rest, in which a uniform upward fluid flow generates a drag force that counteracts the gravitational force (Sundaresan 2003). Although, as in the case of one solid particle immersed in a fluid, other effects arise because of the fluid–solid interactions, such as virtual mass effects and Basset force (Drew 1983), we consider only the total drag force, which can be written as (e.g. Di Felice 1995; Jackson 2000)

$$c_s \frac{\partial \hat{\tau}_{sij}}{\partial x_j} = (1 - \delta_{ij}) K (u_{fi} - u_{si}), \tag{2.8}$$

where K is a well-constrained phenomenological drag function (see Di Felice 1995 and references therein). Thus, (2.7) has the final frame indifferent form:

$$\hat{m}_{si} = -\hat{m}_{fi} = -c_s \frac{\partial p_f}{\partial x_i} + K(u_{fi} - u_{si}). \tag{2.9}$$

The drag function, K, is usually obtained through a generalization of the drag force for a single particle by introducing a voidage function, $f(c_f)$, such as (Di Felice 1995)

$$K = \frac{3}{4} C_D \frac{\gamma_f}{d_s} |\boldsymbol{u_f} - \boldsymbol{u_s}| c_s f(c_f), \tag{2.10}$$

where d_s is the diameter of the solid particles and C_D is the drag coefficient given by Dallavalle (1948) as

$$C_D = \left(0.63 + \frac{4.8}{\sqrt{Re_d}}\right)^2, \tag{2.11}$$

where Re_d is a modified particle Reynolds number, defined as $Re_d = \rho_f d_s |\boldsymbol{u_f} - \boldsymbol{u_s}| / \mu_f = c_f d_s |\boldsymbol{u_f} - \boldsymbol{u_s}| / \nu_f$, where μ_f and ν_f are the dynamic and kinematic viscosity of the fluid phase, respectively. The most common form for the voidage function is $f(c_f) = c_f^{2-\beta}$, with β as a coefficient with values ranging from 3.6 to 3.7 for the viscous and inertial flow regimes, respectively (Di Felice 1994). We use the coefficient proposed by Di Felice (1994) that fits empirically the two regimes as

$$\beta = 3.7 - 0.65 \exp\left[-\frac{(1.5 - \log(Re_d))^2}{2}\right]. \tag{2.12}$$

2.3. *Stress tensor of the fluid phase*

Assuming that the state variables of the governing equation are mean quantities obtained by a Reynolds (1895) average of the equations and using the eddy viscosity concept proposed by Boussinesq (1877) as a model for turbulent fluctuations, the stress tensor for the fluid phase can be written as (Rodi 1983)

$$T_{fij} = -p_f \delta_{ij} + (\mu_f + \mu_T) \left(\frac{\partial u_{fi}}{\partial x_j} + \frac{\partial u_{fj}}{\partial x_i}\right), \tag{2.13}$$

where μ_T is the turbulent or eddy viscosity because of the velocity fluctuations from the mean flow. This eddy viscosity for the case of fluid-particles flows is more complicated than that for the case of pure fluid flows, because the solid particles

modify the structure and intensity of the fluid turbulence, thus altering the transport rate of momentum (Elghobashi & Truesdell 1993). For instance, any slip between phases generates boundary layers around individual particles.

Although there are no general turbulent closures for the fluid phase in the case of two-phase flows, this issue is currently solved by including a source term in the kinetic energy equation of the fluid phase, which represents the irreversible work on the fluid associated with the drag force on the particles (Crowe, Troutt & Chung 1996). Following Crowe (2000), we propose a standard turbulence energy-dissipation model for the turbulence of the fluid phase ($k-\epsilon$ model; Rodi 1983), which includes the work done by the drag force as a production term in both k and ϵ equations. Then, the set of $k-\epsilon$ equations is written as

$$\mu_T = \rho_f c_\mu \frac{k^2}{\epsilon}, \tag{2.14}$$

$$\frac{\partial(\rho_f k)}{\partial t} + \frac{\partial(\rho_f u_{fi} k)}{\partial x_i} = \frac{\partial}{\partial x_i}\left(\frac{\mu_T}{\sigma_k}\frac{\partial k}{\partial x_i}\right) + \mu_T\left(\frac{\partial u_{fi}}{\partial x_j} + \frac{\partial u_{fj}}{\partial x_i}\right)\frac{\partial u_{fi}}{\partial x_j} + K|\boldsymbol{u_f} - \boldsymbol{u_s}|^2 - \rho_f \epsilon, \tag{2.15}$$

$$\frac{\partial(\rho_f \epsilon)}{\partial t} + \frac{\partial(\rho_f u_{fi} \epsilon)}{\partial x_i} = c_{1\epsilon}\frac{\epsilon}{k}\left[\mu_T\left(\frac{\partial u_{fi}}{\partial x_j} + \frac{\partial u_{fj}}{\partial x_i}\right)\frac{\partial u_{fi}}{\partial x_j} + K|\boldsymbol{u_f} - \boldsymbol{u_s}|^2\right] + \frac{\partial}{\partial x_i}\left(\frac{\mu_T}{\sigma_\epsilon}\frac{\partial \epsilon}{\partial x_i}\right) - c_{2\epsilon}\rho_f \frac{\epsilon^2}{k}, \tag{2.16}$$

where k is the kinetic energy of the fluid turbulent motion, and ϵ is the dissipation rate of k. The values of the constants in (2.14)–(2.16) are taken equal to the standard values for a pure fluid: $c_\mu = 0.09$, $c_{1\epsilon} = 1.44$, $c_{2\epsilon} = 1.92$, $\sigma_k = 1.00$ and $\sigma_\epsilon = 1.30$ (Rodi 1983; Pope 2000).

2.4. *Stress tensor of the solid phase*

The stress tensor of the solid particles represents the forces transmitted by direct inter-particle contacts. These forces are well known for two opposite regimes of the granular flow. On the one hand, the dilute and rapid granular flow regime in which the particles interact by binary collisions (Campbell 1990; Goldhirsch 2003), and on the other hand, the dense quasi-static regime in which the onset of the flow is determined by the Mohr–Coulomb condition (Hutter *et al.* 2005). However, the constitutive equation for the intermediate regime in which both collisional and frictional interactions might be important is not well known (Forterre & Pouliquen 2008). In order to take into account these three regimes, we will follow the assumption of Savage (1983) and Johnson & Jackson (1987), who proposed that the stress tensor of the solid particles is represented by the linear sum of a rate-independent quasi-static part, T^s_{sij}, and a rate-dependent collisional part, T^c_{sij}, such as

$$T_{sij} = T^s_{sij} + T^c_{sij}. \tag{2.17}$$

The rate-independent quasi-static part, T^s_{sij}, can be decomposed as

$$T^s_{sij} = -p_s \delta_{ij} + \tau_{sij}, \tag{2.18}$$

where p_s is the solid pressure (assumed isotropic) and τ_{sij} is the solid shear stress tensor. We define the solid pressure as the reaction force that arises in response to the constraint of incompressibility when the solid particles are packed, which in the static

case can be interpreted as the fraction of the weight of the solids that is sustained by direct contacts among solid particles or at boundaries. Accordingly, the solid pressure can be written as

$$p_s(c_s) = \begin{cases} p_s & c_s \geqslant c_o, \\ 0 & c_s < c_o, \end{cases} \tag{2.19}$$

where c_o is the loose packing concentration defined as the lowest stable packing of particles. Mathematically, the inclusion of the closure (2.19) means that one of the two variables, c_s or p_s, will be constant depending on whether the flow is packed or not. When the granular flow is packed, i.e. when it is incompressible, the solid density ρ_s is constant; in contrast, when the granular flow is unpacked, i.e. when it is compressible, p_s is equal to zero. In fact, this model ensures that once the granular flow is unpacked, the maximum concentration that it can acquire is the loose packing value.

The quasi-static solid shear stress tensor, τ_{sij}, is represented by the Mohr–Coulomb condition, which states that the compressible and shear stresses acting in a particular plane over a particular point are related by (e.g. Goodman & Cowin 1971)

$$|\tau_{sij}| = (1 - \delta_{ij})|p_s|\tan\varphi, \tag{2.20}$$

where φ is the internal friction angle. Note that because of the closure of (2.19), the solid shear stress also vanishes when the flow is unpacked.

The rate-dependent collisional part, T^c_{sij}, on the other hand, arises in a rapid sheared flow in which each particle has a random fluctuation of the velocity respect to the mean flow. As this random motion arises from particles collisions, the granular flow is represented in a similar way as the thermal motion of molecules in the kinetic theory of gases, considering additionally the energy loss because of inelastic collisions (Campbell 1990; Goldhirsch 2003). We use the kinetic theory proposed by Jenkins & Savage (1983), in which the collisional stress tensor can be written as

$$T^c_{sij} = -p_c\delta_{ij} + 2\mu_c\dot{\gamma}_{sij}, \tag{2.21}$$

where $\dot{\gamma}_{sij} = (\partial_{x_j}u_{si} + \partial_{x_i}u_{sj})$ is the shear rate tensor, $p_c = \gamma_s f_1(c_s, e)T$ is the collisional pressure, $\mu_c = \gamma_s d_s f_2(c_s, e)\sqrt{T}$ is the collisional viscosity, with $T = \langle u'^2_{si}\rangle/3$ the granular temperature, where u'_{si} is the instantaneous deviation from the mean velocity and $\langle\rangle$ represents an ensemble average. In this model, the parameterizations $f_1(c_s, e)$ and $f_2(c_s, e)$ are equal to

$$f_1(c_s, e) = 2c_s^2(1 + e)g_o(c_s), \quad f_2(c_s, e) = \frac{2}{5\sqrt{\pi}}c_s^2(2 + \alpha)(1 + e)g_o(c_s), \tag{2.22}$$

where e is the coefficient of restitution, α is a parameter equal to one as Lun, Savage & Jeffrey (1984) suggested, and $g_o(c_s)$ is the radial distribution function. We use the function proposed by Lun *et al.* (1984) that is implicit in the work of Bagnold (1954)

$$g_o(c_s) = \left[1 - \left(\frac{c_s}{c_M}\right)^{1/3}\right]^{-1}, \tag{2.23}$$

where c_M is the dense packing concentration equal to 0.64 for spheres (Lun *et al.* 1984). Finally, we relate this model with our representation through the relation between the shear rate and the granular temperature $S = d_s\dot{\gamma}_s T^{-1/2}$, for which $S \approx 1$ in most of the range of the solid concentration (Campbell 2006), so that we consider

$$T = (d_s\dot{\gamma}_s)^2, \tag{2.24}$$

where $\dot{\gamma}_s = \sqrt{1/2|\dot{\gamma}_{sii}^2 - \dot{\gamma}_{sij}\dot{\gamma}_{sji}|}$ is the root of the second invariant of the shear rate tensor.

2.5. *Dimensionless form of the governing equations*

The final system of governing equations is represented by

$$\frac{\partial \rho_n}{\partial t} + \frac{\partial(\rho_n u_{ni})}{\partial x_i} = 0, \quad n = s, f, \tag{2.25}$$

$$\frac{\partial \rho_s u_{si}}{\partial t} + \frac{\partial(\rho_s u_{sj} u_{si})}{\partial x_j} = \rho_s g_i - \frac{\partial p_s}{\partial x_i} + s_{ij}\frac{\partial p_s}{\partial x_j}\tan\varphi + \frac{\partial}{\partial x_j}\left[\mu_c\left(\frac{\partial u_{si}}{\partial x_j} + \frac{\partial u_{sj}}{\partial x_i}\right)\right] - \frac{\partial p_c}{\partial x_i} - c_s\frac{\partial p_f}{\partial x_i} + K(u_{fi} - u_{si}), \tag{2.26}$$

$$\frac{\partial \rho_f u_{fi}}{\partial t} + \frac{\partial(\rho_f u_{fj} u_{fi})}{\partial x_j} = \rho_f g_i - c_f\frac{\partial p_f}{\partial x_i} + \frac{\partial}{\partial x_j}\left[(\mu_f + \mu_T)\left(\frac{\partial u_{fi}}{\partial x_j} + \frac{\partial u_{fj}}{\partial x_i}\right)\right] - K(u_{fi} - u_{si}), \tag{2.27}$$

where $s_{ij} \equiv \mathrm{sgn}(\partial_{x_j} u_{si})$. This system of equations is closed with the saturation constraint $c_s + c_f = 1$, and (2.10)–(2.12), (2.14)–(2.16), (2.19), (2.22)–(2.24). We use the governing equations for studying the collapse of a two-dimensional granular column in a viscous fluid. Previous experimental studies in air (e.g. Lajeunesse *et al.* 2005; Lube *et al.* 2005) have established that the characteristic time scale is $\sqrt{h_o/g}$, independent of the properties of the granular material (grain size, roughness and shape) and of the initial column aspect ratio h_o/x_o, where h_o and x_o are the initial height and length, respectively. As we also apply the equations in cases in which water is the ambient fluid, we define $t_o = \sqrt{h_o/g'}$ as the characteristic time scale, where $g' = (\gamma_s - \gamma_f)/\gamma_s g$ is the reduced gravity. On the other hand, the traditional dam-break problem for flows of water indicates that the characteristic horizontal velocity scale is the gravity wave celerity $u_o = \sqrt{g' h_o}$ (Kármán 1940), so that the characteristic horizontal length scale is $\sim u_o t_o \sim h_o$. In order to have each term of the same order in the conservation of mass equation, u_o and h_o are also chosen as scales for both vertical velocity and length. Using the loose packing density of the solids, $c_o\gamma_s$, and the material density of the fluid, γ_f, as density scales, the following dimensionless variables are obtained:

$$\left.\begin{aligned} \widetilde{t} &= \frac{t}{t_o},\ \widetilde{x}_i = \frac{x_i}{h_o},\ \widetilde{u}_{ni} = \frac{u_{ni}}{u_o},\ \widetilde{\rho}_f = \frac{\rho_f}{\gamma_f},\ \widetilde{\rho}_s = \frac{\rho_s}{c_o\gamma_s},\ \widetilde{p}_s = \frac{p_s}{c_o\gamma_s u_o^2}, \\ \widetilde{p}_c &= \frac{p_c}{c_o\gamma_s u_o^2},\ \widetilde{p}_f = \frac{p_f}{\gamma_f u_o^2},\ \widetilde{k} = \frac{k}{u_o^2},\ \widetilde{\epsilon} = \frac{\epsilon}{u_o^2},\ \widetilde{T} = \frac{T}{u_o^2}, \end{aligned}\right\} \tag{2.28}$$

where $x_1 = x$, $x_2 = y$ are the horizontal and vertical directions, respectively, and $\sim$ denotes scaled variables. Substitution of these variables in the conservation of mass (2.25), and momentum equations (2.26) and (2.27) leads to

$$\frac{\partial \widetilde{\rho}_n}{\partial \widetilde{t}} + \frac{\partial(\widetilde{\rho}_n \widetilde{u}_{ni})}{\partial \widetilde{x}_i} = 0, \quad n = s, f \tag{2.29}$$

$$\frac{\partial \widetilde{\rho}_s \widetilde{u}_{si}}{\partial \widetilde{t}} + \frac{\partial(\widetilde{\rho}_s \widetilde{u}_{sj} \widetilde{u}_{si})}{\partial \widetilde{x}_j} = \widetilde{\rho}_s\frac{g_i}{g'} - \frac{\partial \widetilde{p}_s}{\partial \widetilde{x}_i} + s_{ij}\frac{\partial \widetilde{p}_s}{\partial \widetilde{x}_j}\tan\varphi + \frac{\partial}{\partial \widetilde{x}_j}\left[\frac{1}{Re_c}\left(\frac{\partial \widetilde{u}_{si}}{\partial \widetilde{x}_j} + \frac{\partial \widetilde{u}_{sj}}{\partial \widetilde{x}_i}\right)\right] - \frac{\partial \widetilde{p}_c}{\partial \widetilde{x}_i} - De\frac{c_s}{c_o}\frac{\partial \widetilde{p}_f}{\partial \widetilde{x}_i} + \sqrt{\frac{De}{Ar}}\frac{h_o}{d_s}\frac{\widetilde{K}}{c_o}(\widetilde{u}_{fi} - \widetilde{u}_{si}), \tag{2.30}$$

Set	γ_f (kg m^{-3})	ν_f ($\times 10^{-5}$ m^2 s^{-1})	d_s ($\times 10^{-3}$ m)
1	1.2	1.7	3.0
2	1.2	1.7	0.7
3	1.2	1.7	0.2
4	1000	0.1	3.0
5	1000	0.1	0.7
6	1000	0.1	0.2

TABLE 1. Mean values of material properties and boundary conditions for laboratory and numerical experiments. For each set: $\gamma_s = 2.5\times10^3$ kg m^{-3}, $c_o = 0.6$, $e = 0.95$, $\varphi = 26^o$, $x_o = 0.1$ m for $h_o/x_o \in [1, 4.5]$, $x_o = 0.05$ m for $h_o/x_o \in [5, 16]$, $\Delta x = \Delta y = 7.14 \times 10^{-3}$ m, and $\Delta t = 2.5 \times 10^{-3}$ s.

$$\frac{De}{c_o}\left[\frac{\partial \widetilde{\rho}_f \widetilde{u}_{fi}}{\partial \widetilde{t}} + \frac{\partial(\widetilde{\rho}_f \widetilde{u}_{fj}\widetilde{u}_{fi})}{\partial \widetilde{x}_j}\right] = \widetilde{\rho}_f \frac{De}{c_o}\frac{g_i}{g'} + \frac{De}{c_o}\frac{\partial}{\partial \widetilde{x}_j}\left[\frac{1}{Re_f}\left(\frac{\partial \widetilde{u}_{fi}}{\partial \widetilde{x}_j} + \frac{\partial \widetilde{u}_{fj}}{\partial \widetilde{x}_i}\right)\right] - De\frac{c_f}{c_o}\frac{\partial \widetilde{p}_f}{\partial \widetilde{x}_i} - \sqrt{\frac{De}{Ar}\frac{h_o}{d_s}}\frac{\widetilde{K}}{c_o}(\widetilde{u}_{fi} - \widetilde{u}_{si}), \quad (2.31)$$

where $\widetilde{K} = 3/4(0.63\sqrt{Re_d} + 4.8)^2 c_s c_f^{1-\beta}$. The density number, De, the Archimedes number, Ar, and the Reynolds numbers, Re_c and Re_f, are defined as

$$De = \frac{\gamma_f}{\gamma_s}, \quad Ar = \frac{(\gamma_s - \gamma_f)g d_s^3}{\gamma_f \nu_f^2}, \quad Re_c = \frac{c_o \gamma_s h_o \sqrt{g' h_o}}{\mu_c}, \quad Re_f = \frac{\gamma_f h_o \sqrt{g' h_o}}{\mu_f + \mu_T}. \quad (2.32)$$

3. Methods

3.1. *Experimental procedure*

Experiments were conducted in a 1.5 m long perspex rectangular channel, 0.5 m deep and 0.1 m wide, by suddenly opening a vertical gate that initially holds the granular column of $h_o/x_o \in [1, 8]$. For each set of aspect ratios, we used glass beads of three particle sizes ($d_s = 0.2, 0.7, 3.0$ mm), and air or water as the ambient fluid (the depth of water was 0.45 m), with a total of six sets of experiments listed in table 1.

The physical properties presented in table 1 correspond to the typical mean values of the materials used at 20°C, and we measured the loose packing volume concentration ($c_o = 0.6 \pm 0.2$) as well as the internal friction angle ($\varphi = 26 \pm 3$ deg). The loose packing volume concentration was estimated by measuring the volume of water displaced when a known volume of packed particles is immersed in water. The internal angle of friction was assumed to be equal to the angle of repose, which was estimated by pouring the particles on a rough horizontal plane from a fixed source. The angle below which the heap stays unchanged at rest, and above which surface motion downslope starts was considered as the internal friction angle. This angle is in the range measured in other experimental studies with subspherical glass beads (e.g. Balmforth & Kerswell 2005; Lajeunesse *et al.* 2005).

The experimental procedure can be summarized as follows. The glass beads are poured into the reservoir without agitation or vibration. The channel is illuminated with diffuse back lighting that provides a good contrast for video analysis, and a video camera is carefully aligned along the horizontal direction. The gate is then manually removed by suddenly lifting a rope to release the granular mass that spreads into the

horizontal channel until it comes to rest, while the flow is recorded with the video camera acquiring 50 frames per second. Finally, the resulting movie is processed with Matlab® in order to obtain series of the free surface and the front position of the granular flow. This procedure was conducted twice for each experiment.

As in the numerical simulations the effect of gate removal is not considered, we verified that it is negligible as the time for opening was ∼0.1 s, which corresponds to less than about 5 %–10 % of the typical duration of the experiments in water and air, respectively. We also verified the error in the procedure obtaining $\pm 0.05\ \mathrm{m\,s^{-1}}$ in the front velocity, which corresponds to less than about 4 %–8 % of the typical front velocity in air and water, respectively.

3.2. *Numerical solution*

Before discussing the numerical solution, two important properties of the system of nonlinear second-order partial differential equations (2.29)–(2.31) should be noted. First, as in the case of Navier–Stokes equations, it is not possible to define whether the hyperbolic or parabolic feature of the momentum equations dominates, since the ratio between the rate of convection of the flow to its rate of diffusion (the Péclet number) is not known *a priori*. Then, the discretization method should handle both convection and diffusion terms as a unit (Patankar 1980, pp. 79–80). Second, the inviscid limit of these equations, in which momentum losses are not considered, gives an ill-posed system of equations because some wave celerities acquire complex values, i.e. the inviscid equations are non-hyperbolic, and the numerical solution shows that small-scale phenomenon grows rapidly (Drew 1983; Stewart & Wendroff 1984; Ystrom 2001). Then, viscous terms should be retained in order to have a well-posed system of equations (Drew 1983; Ystrom 2001).

Based on this and on the fact that the pressure fields for both phases are not known, we chose the implicit finite-volume pressure–correction scheme proposed by Patankar (1980) for solving the momentum equations, which is an iterative procedure for calculating the flow field through a way that improves the guessed pressure. This procedure is based on the fact that the pressure field is indirectly specified via the mass continuity equation, so that when the correct pressure field is substituted into the momentum equations, the resulting velocity field satisfies the mass continuity equation (Patankar 1980, pp. 124–126). To prevent numerical instabilities of the velocity field associated with the central difference approximations, the convection and diffusion fluxes were solved with the hybrid scheme, which is a combination of the central difference and upwind schemes, and depends on the Péclet number (Patankar 1980, pp. 88–90). Furthermore, we adopted a closed two-dimensional (vertical–longitudinal) domain with a staggered Cartesian grid, in which the velocity components are calculated for the points lying on the faces of the control volumes, which allows to avoid the difficulties that arise when pressure and velocity fields are calculated at the same location, such as a non-uniform pressure field (Patankar 1980, pp. 118–120).

Regarding to the boundary conditions, a zero mass flow across the walls was considered for both fluid and solid phases because the domain was closed, so that a normal velocity equal to zero was given as a boundary condition to both the pressure-correction and the momentum equations. Additionally, the non-slip boundary condition was considered for the fluid phase, so that the fluid velocity parallel to the walls was equal to zero; and a zero momentum flux across the walls was assumed for the solid phase, so that the gradient of the solids velocity parallel to the walls was equal to zero, which means that solid particles can slip on the walls. Moreover, a wall friction equal to the inner Coulomb friction $\tan\varphi$ was assumed. Finally, as both mean

and fluctuating fluid velocities were zero at the walls, the turbulent kinetic energy, k, was also zero at the walls; in contrast, the dissipation rate ϵ should have been finite (Rodi 1983, pp. 44–45). The usual way to treat the boundary conditions for ϵ is by placing the boundaries out of the viscous wall boundary layer, where the flow is fully turbulent, and assuming that the rate of production and dissipation of k are equal in that point, which also required to know the flow velocity in that point (Rodi 1983, pp. 44–45). The same methodology is no longer valid for two-phase flows because there is not a clear definition of the wall viscous boundary layer within the grains; then, we decided to impose $\epsilon = 0$ at the boundary. Note that no specific treatment of the free-surface boundary conditions of the granular flow is required, because the proposed granular pressure closure (2.19) naturally creates interfaces as it induces the fall of the particles while the flow is not packed, and because the properties of each phase vary in space according to the volume fraction.

The final discretized equations are detailed in the Appendix, for which the solution algorithm for one time step can be summarized as follows. (i) Start the calculation of the fields at the new time step with the solution of the previous time step. (ii) Solve the discretized momentum equations for the fluid phase. (iii) Solve the pressure-correction equation for the fluid phase and correct fluid pressure and velocities (under-relaxed). (iv) Solve the discretized momentum equations for the solid phase. (v) Solve the pressure-correction equation for the solid phase and correct solid pressure and velocities (under-relaxed). (vi) Solve the discretized conservation of mass equation for the solid phase. (vii) Solve the discretized $k-\epsilon$ equations for the fluid phase. (viii) Update collisional pressure and viscosity for the solid phase. (ix) With the new fields, return to step (ii) until a converged solution for both the continuity and momentum equations is satisfied to an acceptable tolerance (difference in velocity between two successive iterations less than 1 mm s^{-1}), for both the fluid and solid phases.

We solved numerically the six sets of experiments presented in table 1, for which the range of initial column aspect ratio was extended up to 16. The horizontal dimension of the computational domain, L, was fixed by the experimental facility (i.e. $L = 1.5$ m); whereas the vertical dimension, H, was chosen as $H = 2h_o$, as we verified that for H larger than $\sim 1.5h_o$, the influence of the boundary condition at the top of the computational grid was negligible. For simplification and because the horizontal dimension of the domain was fixed, independent of the experiment, we used a fixed grid size of $\Delta x = \Delta y = 7.14 \times 10^{-3}$ m (i.e. $L/\Delta x = 210$) and a time step of $\Delta t = 2.5 \times 10^{-3}$ s (i.e. $\sqrt{Lg^{-1}}/\Delta t = 156$), such as $\Delta x/\Delta t = 2.9$ m s^{-1} was about twice the maximum front propagation speed. The details of the numerical set-up for each simulation are also summarized in table 1.

4. Results

4.1. *Dynamics of the granular column collapse and spreading*

In order to characterize the particular dynamics of the granular column collapse and spreading, in figures 1–3, we present the results of laboratory experiments and numerical simulations carried out in air or water with grains size of 3 mm in diameter and columns with $h_o/x_o = 3$.

Figure 1(a,f) shows frames of the dimensionless solid pressure, $\widetilde{p}_s$, the streamlines of the granular flow and a comparison of measured and computed, $c_o^{-1}\int_0^H c_s(\widetilde{x},\widetilde{y})\mathrm{d}\widetilde{y}$, free surface of the granular flow, for three dimensionless times $\widetilde{t}$. Figure 1(g) compares time series of $\widetilde{p}_s$ at the left bottom corner of the column and the column height at the left top, y_T/h_o. Finally, a comparison between measured and simulated time series

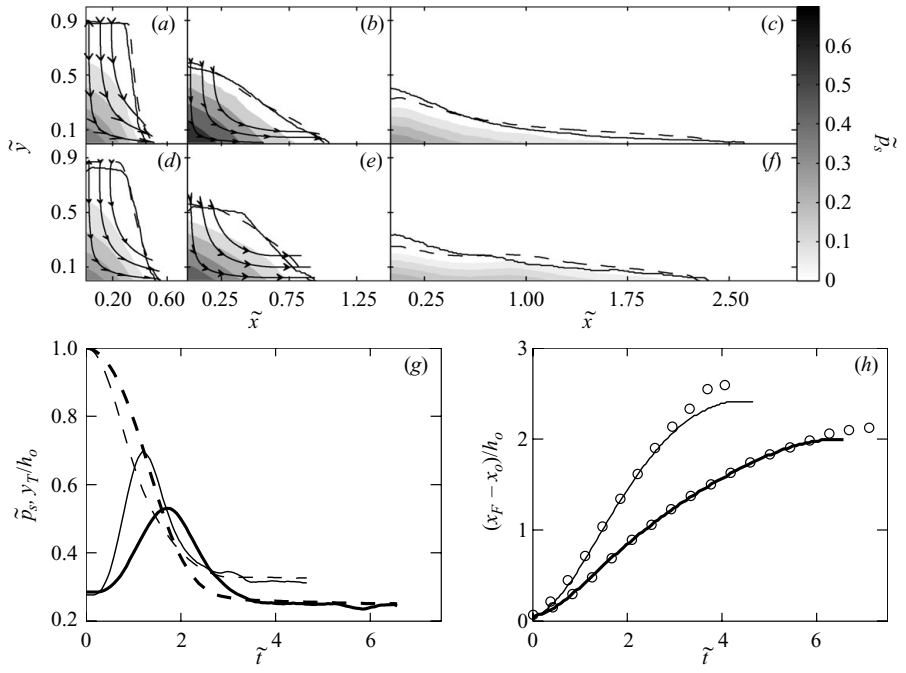

FIGURE 1. Frames of $\widetilde{p}_s$ (contours), streamlines of the granular flow (⟶) and experimental (———) and computed $c_o^{-1}\int_0^{\widetilde{H}} c_s(\widetilde{x},\widetilde{y})\mathrm{d}\widetilde{y}$ (– – –) free surface, for the collapse of grain columns with $d_s = 3$ mm and $h_o/x_o = 3$ in air at (*a*) $\widetilde{t} = 0.5$, (*b*) $\widetilde{t} = 1.0$, (*c*) $\widetilde{t} = 3.0$ and in water at (*d*) $\widetilde{t} = 0.75$, (*e*) $\widetilde{t} = 1.5$, (*f*) $\widetilde{t} = 6.0$. (*g*) Time series of $\widetilde{p}_s$ at the left bottom corner of the column (———), and column height y_T/h_o at the left top (– – –), in air (light lines) and water (dark lines). (*h*) Comparison between simulated (———) and measured (○) time series of $(x_F - x_o)/h_o$, in air (light line) and water (dark line).

of the dimensionless front position, $(x_F - x_o)/h_o$, is shown in figure 1(*h*). Figure 1 illustrates the mechanisms of the granular collapse. The granular flow is first driven by the horizontal solid pressure gradient; however, the wall boundary condition curves the streamlines and tilts the isobars, inducing the fall of the top of the column where solid pressure is equal to zero (figures 1*a* and 1*d*). The vertical collapse progressively increases the solid pressure at the base of the column (figure 1*g*), thus transferring vertical to horizontal solid-phase momentum (figures 1*b* and 1*e*). As a consequence, the flow is mostly non-hydrostatic since $\widetilde{p}_s$ is different than y_T/h_o (figure 1*g*). Finally, the granular motion ends in a static state because of the Mohr–Coulomb condition (figures 1*c*, 1*f*, and 1*h*).

Figure 2 shows contour graphs of the dimensionless solid and fluid velocities, $\widetilde{\boldsymbol{u}}_s$, $\widetilde{\boldsymbol{u}}_f$, kinetic energy of the fluid turbulent motion, $\widetilde{k}$, and granular temperature, $\widetilde{T}$, in air at $\widetilde{t} = 1.5$ (left panels) and in water at $\widetilde{t} = 2.0$ (right panels). It is observed static and dynamic regions of the granular flow due to the Mohr–Coulomb condition (figures 2*a* and 2*b*), with a surface above which material slides down and below which grains remain almost static, while in the front area the movement can be described as a plug-like flow. Furthermore, the movement of the surrounding fluid is induced by the solid particles through two mechanisms: drag interactions and volume interchanges. On the one hand, the drag force induces about the same fluid velocity as the solid particles (magnitude and direction), except at the walls where the fluid velocity is

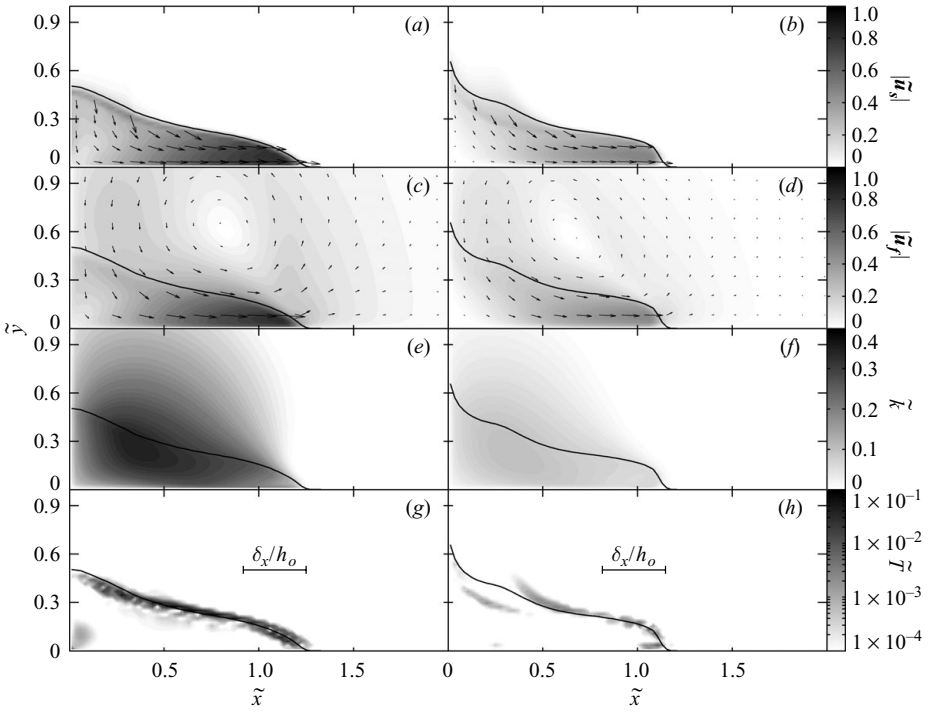

FIGURE 2. Numerical results of grain columns with $d_s = 3$ mm and $h_o/x_o = 3$ in air at $\widetilde{t} = 1.5$ (left panels) and water at $\widetilde{t} = 2.0$ (right panels). Spatial variation of the magnitude (contour) and direction (arrows) of $\widetilde{\boldsymbol{u}}_s$ (*a*,*b*) and of $\widetilde{\boldsymbol{u}}_f$ (*c*,*d*). Contour graph of $\widetilde{k}$ (*e*,*f*) and $\widetilde{T}$ (*g*,*h*), and horizontal dimensions of CV, $\delta_x/h_o = 0.3$ (*g*,*h*). The black solid line represents the dimensionless free surface of the granular flow, $c_o^{-1}\int_0^{\widetilde{H}} c_s(\widetilde{x},\widetilde{y})\mathrm{d}\widetilde{y}$.

constrained by the no-slip fluid boundary condition (figures 2*c* and 2*d*). On the other hand, because of the volume continuity ($c_s + c_f = 1$), the ambient fluid occupies the space left by the solid particles, thus generating the large fluid recirculation patterns shown in figures 2*c* and 2*d*. Finally, fluid turbulence is generated in the whole granular flow and is transported by the fluid to zones where there are no solid particles (figures 2*e* and 2*f*), whereas granular temperature is generated mainly at the free surface of the granular flow (figures 2*g* and 2*h*). As a consequence, the eddy viscosity of the fluid phase, μ_T, acts in a much larger volume than the collisional viscosity of the solid phase, μ_c, so that fluid turbulence is expected to be more important than particles collisions, although $Re_f \sim Re_c \sim 100$.

The dimensionless front position in figure 3(*a*,*b*) shows the well-known acceleration, constant velocity and deceleration regimes, which characterize the dynamics of granular column collapses (e.g. Lajeunesse *et al.* 2005; Lube *et al.* 2005). To understand the constant velocity regime, the force balance at the front was studied by integrating (2.30) in the Lagrangian control volume, CV, defined between $\widetilde{x} = (x_F - \delta_x)/h_o$ and $\widetilde{x} = x_F/h_o$, and the whole vertical domain (δ_x is defined in figures 2*g* and 2*h*, and $\delta_x/h_o = 0.3$). The horizontal solid-phase momentum equation (2.30) was written for the Lagrangian coordinates $\widetilde{t}' = \widetilde{t}$, $\widetilde{y}' = \widetilde{y}$ and $\widetilde{x}' = \widetilde{x} - \widetilde{u}_F\widetilde{t}$, with $\widetilde{u}_F = u_F/u_o$ constant. Figure 3(*c*,*d*) shows the time series of volume-integrated dimensionless terms of the horizontal solid-phase momentum equation: Lagrangian momentum advection ($-\partial_{\widetilde{x}'}[\widetilde{\rho}_s(\widetilde{u}_s - \widetilde{u}_F)\widetilde{u}_s]$), solid pressure gradient ($-\partial_{\widetilde{x}'}\widetilde{p}_s$), Coulomb

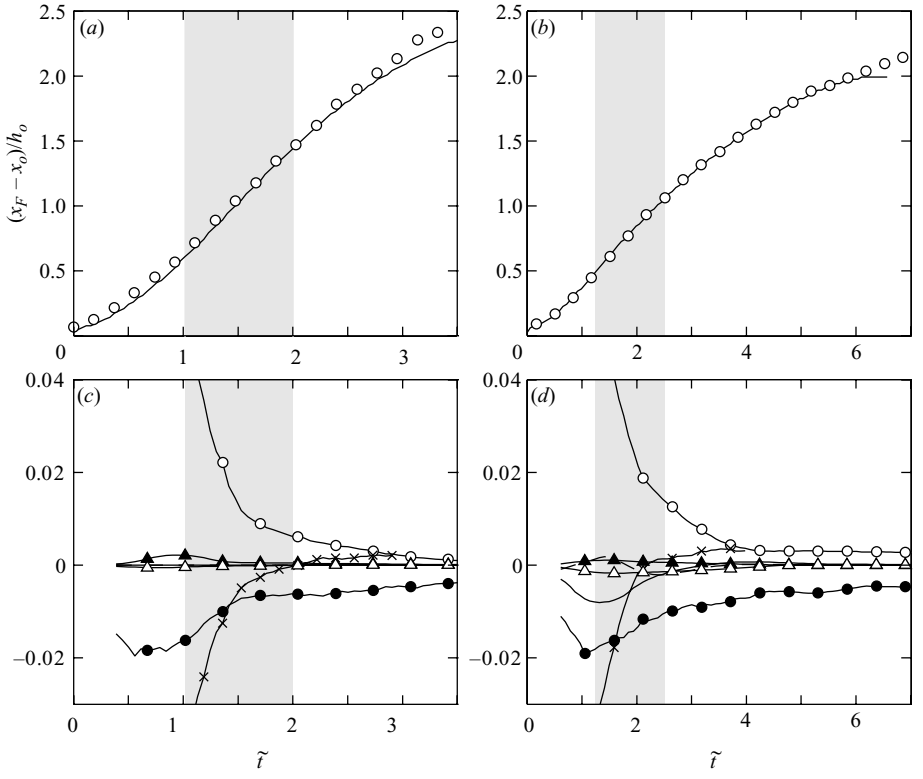

FIGURE 3. Results of grain columns with $d_s = 3$ mm and $h_o/x_o = 3$ in air (left panels) and water (right panels). (*a*,*b*) Measured (○) and simulated (———) time series of $(x_F - x_o)/h_o$. (*c*,*d*) Temporal variation of the horizontal forces integrated over CV: advection $-\partial_{\tilde{x}'}[\widetilde{\rho}_s(\widetilde{u}_s - \widetilde{u}_F)\widetilde{u}_s]$ (—×—), solid pressure gradient $-\partial_{\tilde{x}'}\widetilde{p}_s$ (—○—), Coulomb friction $s_{xy}\partial_{\tilde{y}'}\widetilde{p}_s\tan\varphi$ (—●—), collisional pressure gradient $-\partial_{\tilde{x}'}\widetilde{p}_c$ (—▲—), collisional shear stress $\partial_{\tilde{x}'}[2Re_c^{-1}\partial_{\tilde{x}'}\widetilde{u}_s] + \partial_{\tilde{y}'}[Re_c^{-1}(\partial_{\tilde{y}'}\widetilde{u}_s + \partial_{\tilde{x}'}\widetilde{v}_s)]$ (—△—), fluid pressure gradient $-Dec_s/c_o\partial_{\tilde{x}'}\widetilde{p}_f$ (– – –) and drag force $\sqrt{De\ h_o/(Ar\ d_s)}\widetilde{K}/c_o[\widetilde{u}_f - \widetilde{u}_s]$ (———). Shaded areas correspond to the constant velocity regime.

friction ($s_{xy}\partial_{\tilde{y}'}\widetilde{p}_s\tan\varphi$), collisional pressure gradient ($-\partial_{\tilde{x}'}\widetilde{p}_c$), collisional shear stress ($\partial_{\tilde{x}'}[2Re_c^{-1}\partial_{\tilde{x}'}\widetilde{u}_s] + \partial_{\tilde{y}'}[Re_c^{-1}(\partial_{\tilde{y}'}\widetilde{u}_s + \partial_{\tilde{x}'}\widetilde{v}_s)]$), fluid pressure gradient ($-Dec_s/c_o\partial_{\tilde{x}'}\widetilde{p}_f$) and drag force ($\sqrt{De\ h_o/(Ar\ d_s)}\widetilde{K}/c_o[\widetilde{u}_f - \widetilde{u}_s]$). Note that because Lagrangian momentum advection is calculated with a constant front speed, this is only valid in the constant velocity regime (shaded areas in figure 3).

The temporal variation of the horizontal forces integrated over CV shows that the force balance, for the case of the larger particles considered, is described mainly by the balance between horizontal pressure gradient and Coulomb friction (figures 3*c* and 3*d*); however, as shown in the following sections, the relative importance of these forces on the balance changes as a consequence of the particle diameter and fluid properties.

4.2. *Role of the solid pressure and Coulomb friction*

In order to identify the solid pressure and Coulomb friction effects on granular flow dynamics, we carried out two types of numerical experiments without both fluid and particles collisions, either with or without Coulomb friction. The results of the

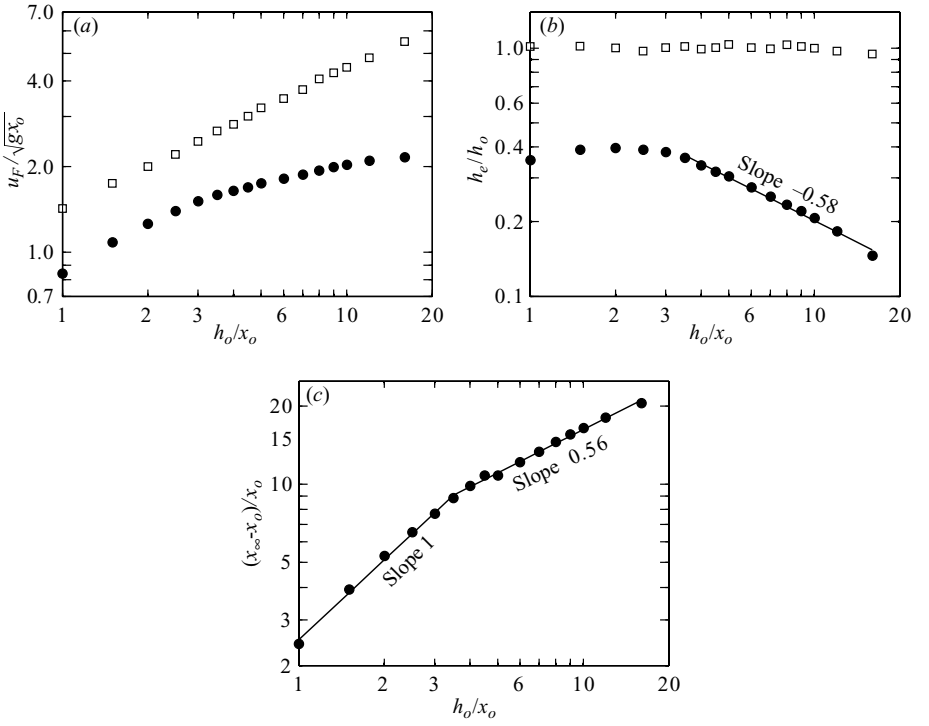

FIGURE 4. Results of numerical experiments without fluid and particles collisions. (*a*) Dimensionless front speed $u_F/\sqrt{gx_o}$ and (*b*) ratio h_e/h_o, as a function of h_o/x_o, for both sets with (●) and without (□) Coulomb friction. (*c*) Dimensionless runout distance, $(x_\infty - x_o)/x_o$, as a function of h_o/x_o, for the case with Coulomb friction (●).

dimensionless front speed in the constant velocity regime, $u_F/\sqrt{gx_o}$, as a function of h_o/x_o, are presented in figure 4(*a*). They show that, as expected from energy considerations, the front speed for the frictionless case is larger than that for the case with friction. Moreover, whereas u_F depends on h_o/x_o for the frictional case (figure 4*a*), $u_F \approx \sqrt{2gh_o}$ in the case without friction, which corresponds to the speed of free fall of the grains from a high h_o. Thus, for the frictionless case, the solid pressure deviates the motion of the granular flow without influencing its speed. As a result, in order to quantify the Coulomb friction effect, we define an equivalent height, h_e, as

$$h_e = h_e(\tan\varphi, h_o/x_o) = \frac{u_F'^2}{2g}, \tag{4.1}$$

where u_F' refers to the front speed without fluid and particles collisions. The ratio h_e/h_o and the dimensionless runout distance, $(x_\infty - x_o)/x_o$, as a function of h_o/x_o, are shown in figures 4(*b*) and 4(*c*), respectively. Both curves show a break in slope at $h_o/x_o \approx 3$, and the runout distance is in quite good agreement with the experimental scaling laws found by Balmforth & Kerswell (2005), Lube *et al.* (2005) and Lajeunesse *et al.* (2005), among others. These numerical experiments show that the physical origin of the break in slope for the dimensionless runout distance is the Coulomb friction ($\tan\varphi$); however, the two-dimensional non-hydrostatic feature of the flow complicates the analysis, so that it is not possible to obtain a direct algebraic expression to compute neither h_e/h_o nor $(x_\infty - x_o)/x_o$ as a function of $\tan\varphi$.

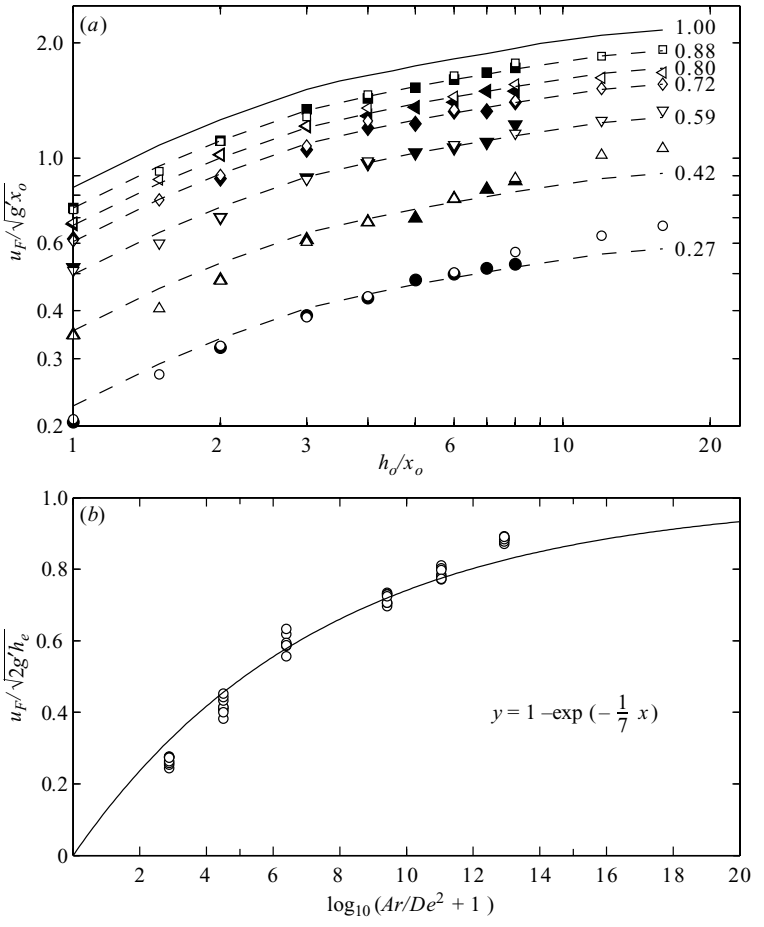

FIGURE 5. (*a*) Results of dimensionless front speed, $u_F/\sqrt{g'x_o}$, as a function of h_o/x_o, for experiments of table 1: set 1 (□), set 2 (◁), set 3 (◇), set 4 (▽), set 5 (△) and set 6 (○). White and black marks are numerical and experimental results, respectively. The dashed lines were obtained by multiplying the results curve without fluid and particles collisions (———) by the factor indicated. (*b*) Froude number, $Fr = u_F/\sqrt{2g'h_e}$, as a function of $\log_{10}(Ar/De^2 + 1)$, for the six sets of experimental measurements of table 1 (○). The best fit is represented by the solid line that preserves the physical limits $Fr = 0$ for $\gamma_s = \gamma_f$, and $Fr = 1$ defined without fluid.

4.3. *Role of the ambient fluid*

The six sets of experiments summarized in table 1 are used for studying the role of the ambient fluid on the granular flow dynamics. We chose the front speed in the constant velocity regime to describe the granular flow because it is more sensitive to the ambient fluid effects. Figure 5(*a*) shows a comparison of simulated and measured dimensionless front speed, $u_F/\sqrt{g'x_o}$, as a function of h_o/x_o, for the six sets of experiments. A good agreement is observed without fitting any parameter on the model, thus validating the system of governing equations proposed. Furthermore, the results of figure 5(*a*) suggest that the dependence between u_F and h_o/x_o obtained for the case without fluid is also present when the ambient fluid is considered. This is shown in figure 5(*a*) by the dashed lines that were obtained by multiplying the results curve obtained without fluid and particles collisions (black solid line) by a factor that

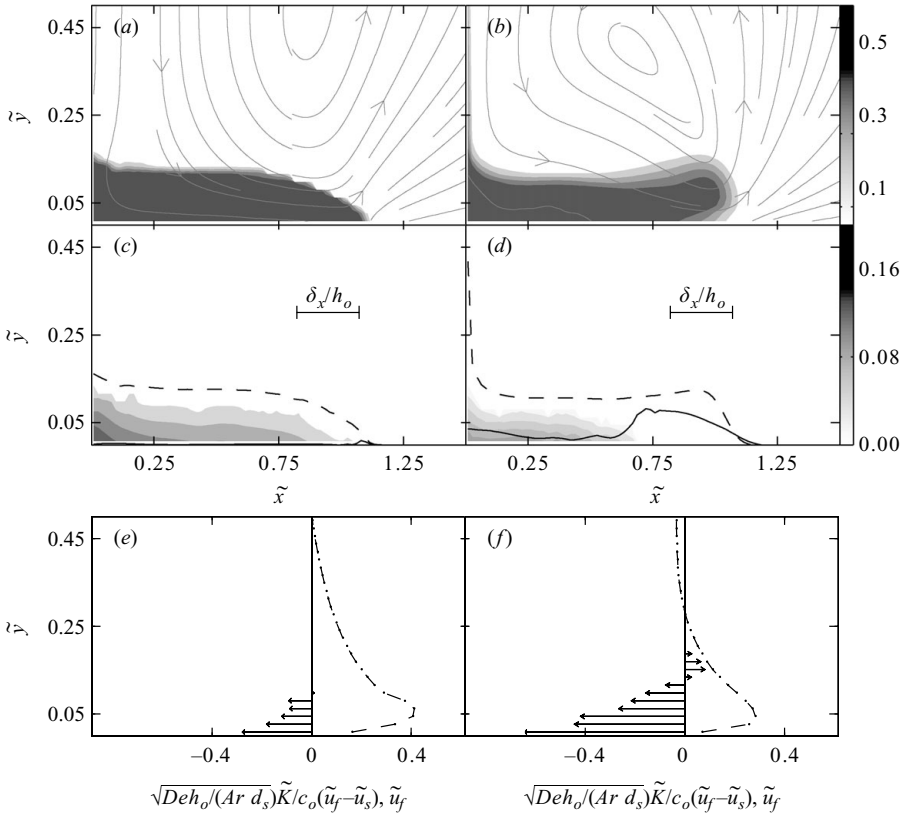

FIGURE 6. Numerical results of grain columns with $d_s = 0.7$ mm and $h_o/x_o = 8$ in air at $\widetilde{t} = 2.0$ (left panels) and water at $\widetilde{t} = 3.5$ (right panels). (*a*,*b*) Contours of c_s with the streamlines of fluid velocity (⟶). (*c*,*d*) Contours of $\widetilde{p}_s$, computed free surface $c_o^{-1}\int_0^{\widetilde{H}} c_s(\widetilde{x},\widetilde{y})\mathrm{d}\widetilde{y}$ (– – –), non-hydrostatic fluid pressure at the bottom of the reservoir dimensionless by $c_o\gamma_s g' h_o$ (———) and horizontal dimensions of CV, $\delta_x/h_o = 0.3$. (*e*,*f*) Dimensionless horizontal fluid velocity, $\widetilde{u}_f$ (– · – ·), and drag force, $\sqrt{De\ h_o/(Ar\ d_s)}\widetilde{K}/c_o[\widetilde{u}_f - \widetilde{u}_s]$ (→), profiles in the front area.

fits each set of experiments. Therefore, the front speed can be written as

$$u_F = Fr\sqrt{2g'h_e}, \tag{4.2}$$

where Fr is a Froude number, and h_e is calculated from the numerical experiments without fluid and particles collisions (4.1). On the other hand, in the dimensional analysis of § 2, the dimensionless groups that weight the interaction terms of (2.30) were introduced: De, Ar, c_s/c_o, $\sqrt{h_o/d_s}$ and $\widetilde{K}/c_o$. The last three groups depend on the initial and boundary conditions, and from figure 5(*a*) they are contained in h_e, at least for the laboratory scale considered. Thus, $Fr = Fr(De, Ar)$ only depends on the solid particle diameter and fluid properties. Experimental front velocities are used to test this hypothesis, and figure 5(*b*) shows the best-fit curve that relates Fr and one function of De and Ar, preserving the physical limits $Fr = 0$ for $\gamma_s = \gamma_f$ and $Fr = 1$ defined without fluid.

Note that even if the front speed is made dimensionless with g', the ambient fluid effects cannot be restricted to the buoyancy force (figure 5), and it is required to analyse the hydrodynamic fluid pressure and drag interactions to characterize

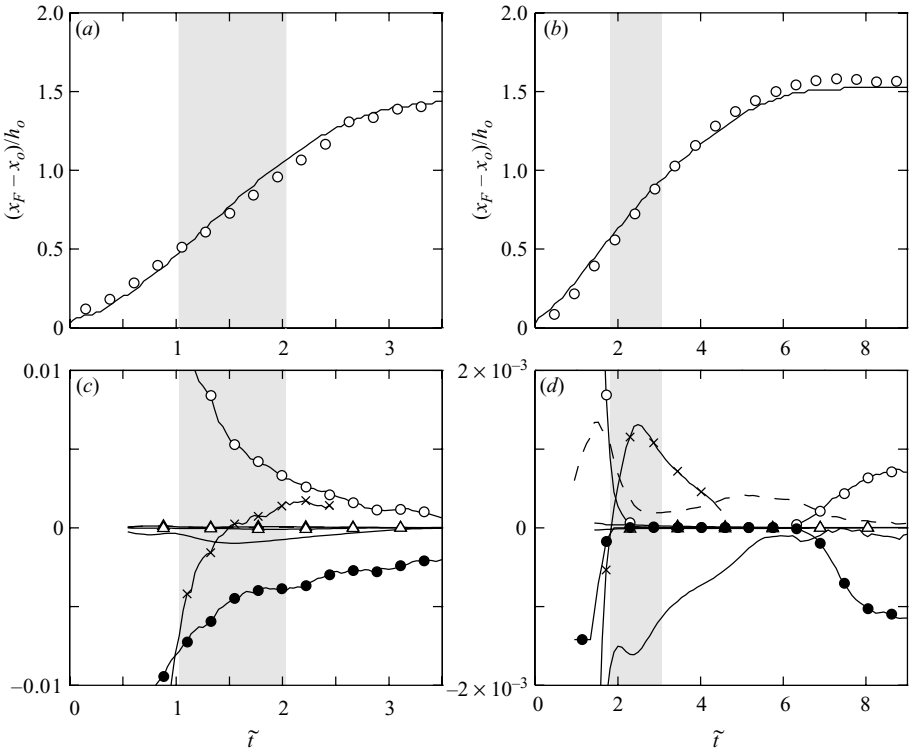

FIGURE 7. Results of grain columns with $d_s = 0.7$ mm and $h_o/x_o = 8$ in air (left panels) and water (right panels). (*a*,*b*) Measured (○) and simulated (———) time series of $(x_F - x_o)/h_o$. (*c*,*d*) Temporal variation of the horizontal forces integrated over CV: advection $-\partial_{\tilde{x}'}[\widetilde{\rho}_s(\widetilde{u}_s - \widetilde{u}_F)\widetilde{u}_s]$ (—×—), solid pressure gradient $-\partial_{\tilde{x}'}\widetilde{p}_s$ (—○—), Coulomb friction $s_{xy}\partial_{\tilde{y}'}\widetilde{p}_s \tan\varphi$ (—●—), collisional pressure gradient $-\partial_{\tilde{x}'}\widetilde{p}_c$ (—▲—), collisional shear stress $\partial_{\tilde{x}'}[2Re_c^{-1}\partial_{\tilde{x}'}\widetilde{u}_s] + \partial_{\tilde{y}'}[Re_c^{-1}(\partial_{\tilde{y}'}\widetilde{u}_s + \partial_{\tilde{x}'}\widetilde{v}_s)]$ (—△—), fluid pressure gradient $-Dec_s/c_o\partial_{\tilde{x}'}\widetilde{p}_f$ (– – –) and drag force $\sqrt{De\ h_o/(Ar\ d_s)}\widetilde{K}/c_o[\widetilde{u}_f - \widetilde{u}_s]$ (———). Shaded areas correspond to the constant velocity regime.

accurately the role of the ambient fluid on granular flow dynamics. Therefore, it is instructive to examine in more detail the spatial and temporal variation of quantities involved in the balance of forces at the front.

Figure 6 shows the results of columns with $h_o/x_o = 8$ and grains of 0.7 mm, in air at $\widetilde{t} = 2.0$ (left panels) and in water at $\widetilde{t} = 3.5$ (right panels). This figure synthesises the role of the ambient fluid. The grains are not packed at the front (figures 6*a* and 6*b*) because their weight is held by both hydrostatic and hydrodynamic fluid pressure (figures 6*c* and 6*d*). Thus, the solid pressure as well as the Coulomb friction is zero in this area (figures 6*c* and 6*d*). This effect is larger in water than in air, suggesting that the magnitude of the fluid pressure fluctuations depends on the fluid density, that is, it is described by De. Even when there is no Coulomb friction at the front, the solid-phase movement may decelerate, as the increase of fluid pressure is caused by momentum transfer through drag interactions, and because the no-slip fluid boundary condition imposes small speed regions near the walls (figures 6*e* and 6*f*).

Figure 7(*a*,*b*) shows measured and simulated time series of $(x_F - x_o)/h_o$, and figure 7(*c*,*d*) shows the time series of volume-integrated dimensionless terms of the

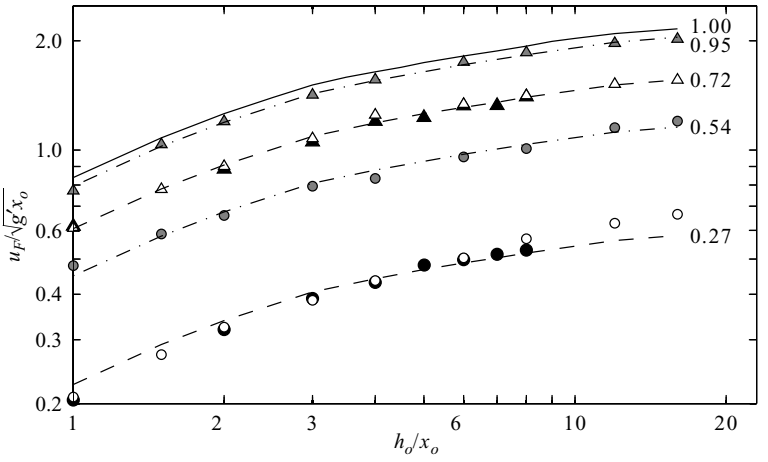

FIGURE 8. Results of $u_F/\sqrt{g'x_o}$ as a function of h_o/x_o, for set 3 (△) and set 6 (○) of table 1. White and grey marks are numerical results with and without fluid turbulence, respectively, and black marks are experimental measurements. The dashed lines were obtained by multiplying the results curve without fluid and particles collisions (———) by the factor indicated.

horizontal solid-phase momentum equation for the experiments presented in figure 6. The temporal variation of the horizontal forces shows that the force balance is described by different interacting forces that depend on the nature of the ambient fluid. In air, the movement is mainly driven by solid pressure gradient, while Coulomb friction (and drag to a lesser extent) counteracts the movement (figure 7*c*). In contrast, the movement in water is mainly driven by momentum advection (and fluid pressure gradient to a lesser extent), while drag counteracts the movement (figure 7*d*). The deceleration phase starts when solid pressure gradient is not large enough against Coulomb friction in air (figure 7*c*), and when advection is not large enough against drag in water (figure 7*d*). In both cases of air and water, the granular motion ends in a static state owing to Coulomb friction.

An important issue of the model that deserves a further analysis is the turbulence of the fluid-phase, as in both cases of air and water drag forces coupled with the wall fluid viscous effects counteract the solid movement (figures 6*e* and 6*f*), so that near-wall viscous effects seem to be important. Figure 8 shows a sensitivity analysis of the results for the smallest particles considered comparing simulations with and without fluid turbulence. It is observed that the front speed increases considerably if the fluid turbulence is not considered, with an increase in speed, calculated as $(u''_F - u_F)/u_F$ with u''_F being the front speed without turbulence, of about 32% in the case of air and of about 100% in the case of water (figure 8). This sensitivity analysis shows that apart from representing accurately the interaction mechanisms between the phases, the dynamic of each phase has to be properly described.

5. Discussion

The two-phase equations for compressible granular flows derived in this paper provide a straightforward way to take into account properly the main forces that describe the solid-phase dynamics: the constituent stresses and the interaction forces

with the ambient fluid. These equations cover the whole solid concentration range between dense granular flows to suspended flows. In order to show that this theory correctly represents the dynamics of two-phase flows, only values taken from the literature for the various parameters of the conceptual model were used when doing the comparison with the experimental measurements (figure 5*a*).

The particular dynamics of the collapse and spreading of a two-dimensional granular column in air or water was successfully solved for a wide range of column aspect ratios, $h_o/x_o \in [1, 16]$. A key feature of the governing equations is the representation of the rate-independent quasi-static part of constituent stresses of the solid particles defined by (2.19) and (2.20), which induces the fall of the particles while the flow is not packed, and creates static and dynamic regions during the granular column collapse because of the Mohr–Coulomb condition (figure 2). Moreover, the inherent non-hydrostatic feature of the governing equations allows the handling of the reported problem in the shallow water equations for high aspect ratios (e.g. Larrieu *et al.* 2006).

By introducing $h_e = h_e(\tan\varphi, h_o/x_o)$ from numerical experiments without fluid and particles collisions (figure 4*b*), the effects of $\tan\varphi$ and h_o/x_o were subtracted, allowing the analysis of the role of the ambient fluid on gravitational granular flow dynamics. Buoyancy is the direct and simplest consequence of the presence of an ambient fluid; however, experimental measurements cannot be explained if the hydrodynamic fluid pressure and drag interactions are not included in the analysis. In fact, fluid pressure gradient and drag interaction terms in (2.30) are coupled and act on the granular flow dynamics. This is shown in figure 5(*b*), in which the best fit for the experimental measurements was found with a combination of De and Ar, which are dimensionless numbers that weight the fluid pressure gradient and the drag terms in (2.30) at the laboratory scale considered. The magnitude of the fluid pressure fluctuations at the flow front is described by De, while the magnitude of the momentum transfer by drag interactions is described by Ar. The combination of both dimensionless numbers determines the dominant terms that describe the force balance during the constant front velocity regime. In air, the dominant dynamical balance results from solid pressure gradient and Coulomb friction (figure 7*c*), because the hydrodynamic fluid pressure that results from volume interchanges and momentum transfer by drag interactions, is not large enough to support the reduced weight of the solid particles (figure 6*c*). In contrast, in the case of water in which the fluid pressure fluctuations are larger, the local behaviour change to a dense suspension for the smaller particles (d_s equal to 0.2–0.7 mm), because the increase of momentum transfer by drag interactions results in an increase of the hydrodynamic fluid pressure that finally support the reduced weight of the solid particles (figure 6*d*), thus resulting in the dominant dynamical balance described by advection and drag forces (figure 7*d*). Furthermore, in cases of both air and water, drag forces coupled with the wall fluid viscous effects counteract the solid movement (figures 6*e* and 6*f*); in this context, fluid turbulence is particularly important and has to be considered in the analysis (figure 8), that is, the problem is taken back to fluid turbulence, which is a fundamental issue in fluid mechanics.

As the interaction mechanisms cannot be restricted to buoyancy or volume exchanges, arguments of low fluid density (Campbell 2006) or constant solid bulk density (Hutter *et al.* 2005) are not enough to neglect the ambient fluid effects. For instance, consider the case of a dense granular flow, for which particles collisions can be ignored, immersed in a real fluid with very low material density (*dry dense granular*

flows), the equations of motion for the solid phase (2.26) reduce to

$$\frac{\partial \rho_s u_{si}}{\partial t} + \frac{\partial (\rho_s u_{sj} u_{si})}{\partial x_j} = \rho_s \frac{g_i}{g} - \frac{\partial p_s}{\partial x_i} + s_{ij} \frac{\partial p_s}{\partial x_j} \tan\varphi. \tag{5.1}$$

Some features of dry dense granular flows can be deduced from these equations. First, the motion depends neither on the fluid phase nor on the solid particle diameter. Second, dry dense granular flows do not reach a uniform steady-state flow regime. If this is the case, the left-hand side terms of (5.1) as well as the horizontal pressure gradient are zero, resulting in the pressure distribution of the static case. If there is motion, the only way to balance gravity and pressure forces is by flow acceleration. As a consequence, to explain the widely reported uniform steady-state flow regime of dry dense granular flows found in different experimental configurations (e.g. GDR MiDi 2004; Forterre & Pouliquen 2008), an additional sink of momentum has to be considered. Although particles collisions may provide the sink of momentum required to balance gravity and pressure forces, the uniform steady-state flow regime for dry dense granular flows can also be explained by drag forces that transfer momentum from solid to fluid phases. This transfer indirectly allows the fluid turbulence to contribute in the solid-phase force balance, as fluid turbulence decreases the fluid velocity, thus increasing drag forces that finally counteract the gravity in the solid-phase force balance. Furthermore, analyses made by Cassar, Nicolas & Pouliquen (2005) and Forterre & Pouliquen (2008), without invoking explicitly the ambient fluid effects, indirectly consider drag forces on the falling time scale of the particles used to derive friction laws for uniform steady avalanches. That is, even with ambient air, the fluid effects that are commonly ignored could become strong enough to explain, for instance, the uniform steady-state flow regime.

The results presented in this article give insights into the influence of the interstitial fluid effects on the dynamics of granular flows, which are one of the *pressing concerns* listed by Campbell (1990, 2006). Further works will focus on heterogeneous (i.e. polydisperse) gravitational granular flows and their associated segregation effects.

The first author acknowledges the financial support from Doctoral fellowship granted by CONICYT (Chile) and the complement granted by the project ECOS-CONICYT C06U01 (France-Chile). We thank Alberto de la Fuente, Ramón Fuentes and Benjamin van Wyk de Vries for their helpful comments on an earlier draft. We also wish to thank the anonymous reviewers for their constructive and critical comments.

Appendix. Numerical scheme

Each of the governing equations can be written in the general convection-diffusion transport equation with source terms:

$$\frac{\partial \rho \phi}{\partial t} + \frac{\partial (\rho u_j \phi)}{\partial x_j} = \frac{\partial}{\partial x_j} \left(\Gamma \frac{\partial \phi}{\partial x_j} \right) + S, \tag{A 1}$$

where ρ is the density, ϕ is the dependent variable, Γ is the diffusion coefficient and S is the source term. The particular representation of each term in the context of the governing equations (2.15)–(2.16) and (2.25)–(2.27) is listed in table 2.

Following Patankar (1980), each governing equation was discretized using both the hybrid scheme (Patankar 1980, pp. 88–90) and the linearization procedure for the

Equation	ρ	ϕ	Γ	S
(2.15)	ρ_f	k	μ_T/σ_k	$\mu_T(\partial_{x_j}u_{fi}+\partial_{x_i}u_{fj})\partial_{x_j}u_{fi}+K\lvert\mathbf{u_f}-\mathbf{u_s}\rvert^2-\rho_f\epsilon$
(2.16)	ρ_f	ϵ	μ_T/σ_ϵ	$c_{1\epsilon}\epsilon/k[\mu_T(\partial_{x_j}u_{fi}+\partial_{x_i}u_{fj})\partial_{x_j}u_{fi}+K\lvert\mathbf{u_f}-\mathbf{u_s}\rvert^2]-c_{2\epsilon}\rho_f\epsilon^2/k$
(2.25)	γ_s	c_s	-	-
(2.26)	ρ_s	u_{si}	μ_c	$\rho_s g_i-\partial_{x_i}p_s+s_{ij}\partial_{x_j}p_s\tan\varphi-\partial_{x_i}p_c-c_s\partial_{x_i}p_f+K(u_{fi}-u_{si})$
(2.27)	ρ_f	u_{fi}	$\mu_f+\mu_T$	$\rho_f g_i-c_f\partial_{x_i}p_f-K(u_{fi}-u_{si})$

TABLE 2. Particular representation of the density, ρ, the dependent variable, ϕ, the diffusion coefficient, Γ, and the source term, S, for each equation.

source terms (Patankar 1980, pp. 48–49). The final two-dimensional discretization equation is written generically as

$$\left.\begin{aligned}
&a_P\phi_P=a_E\phi_E+a_W\phi_W+a_N\phi_N+a_S\phi_S+b,\\
&a_E=\|-F_e,\,D_e-F_e/2,0\|,\;a_W=\|F_w,\,D_w+F_w/2,0\|,\\
&a_N=\|-F_n,\,D_n-F_n/2,0\|,\;a_S=\|F_s,\,D_s+F_s/2,0\|,\\
&a_P=a_E+a_W+a_N+a_S+a_P^o-S_P\Delta x\Delta y+(F_e-F_w)+(F_n-F_s),\\
&a_P^o=\rho_P^o\Delta x\Delta y/\Delta t,\;b=S_C\Delta x\Delta y+a_P^o\phi_P^o,
\end{aligned}\right\}\qquad(A\,2)$$

where the sub-index with the upper-case letter $k=E, W, N, S$ refers to the quantities evaluated at the node east, west, north, south of the central node P; the sub-index with the lower-case letter $l=e, w, n, s$ refers to the quantities evaluated on the face east, west, north, south of the control volume P; the upper-index $()^\circ$ refers to the value of the quantities evaluated in the previous time step;$\|\ \|$ stands for the largest of the quantities within it; S_C and S_P arise from the linearization of the source term $S=S_P\phi_P+S_C$; and the convective, F_l, and diffusive, D_l, fluxes are

$$\left.\begin{aligned}
&F_e=(\rho u)_e\Delta y,\;F_w=(\rho u)_w\Delta y,\;F_n=(\rho u)_n\Delta x,\;F_s=(\rho u)_s\Delta x,\\
&D_e=\Gamma_e\Delta y/\Delta x,\;D_w=\Gamma_w\Delta y/\Delta x,\;D_n=\Gamma_n\Delta x/\Delta y,\;D_s=\Gamma_s\Delta x/\Delta y.
\end{aligned}\right\}\qquad(A\,3)$$

Note that the source terms of the discretized momentum equations (2.26) and (2.27) contain the pressure that is unknown (table 2), so that the mass continuity equations have to be included in order to close the system of equations. For doing this, we followed the iterative SIMPLE (Semi-Implicit Method for Pressure-Linked Equations) algorithm explained in detail in Chapter 6 of Patankar (1980). In this methodology, the pressure and velocities are written as

$$p=p^*+p',\quad u=u^*+u',\quad v=v^*+v',\qquad(A\,4)$$

where $()^*$ denotes guessed values (or values of the previous iteration) and $()'$ denotes correction values. Using p^*, the velocities u^* and v^* are obtained by solving the momentum equations. Then, the correction for the pressure p' is obtained from the pressure-correction equation given by (Patankar 1980, pp. 124–126)

$$\left.\begin{aligned}
&a_P p'_P=a_E p'_E+a_W p'_W+a_N p'_N+a_S p'_S+b,\\
&a_E=\rho_e d_e\Delta y,\;a_W=\rho_w d_w\Delta y,\;a_N=\rho_n d_n\Delta x,\;a_S=\rho_s d_s\Delta x,\\
&d_e=\Delta y/a_e^u,\;d_w=\Delta y/a_w^u,\;d_n=\Delta x/a_n^v,\;d_s=\Delta x/a_s^v,\\
&a_P=a_E+a_W+a_N+a_S,\\
&b=(\rho_P^o-\rho_P)\Delta x\Delta y/\Delta t+(F_w-F_e)+(F_s-F_n),
\end{aligned}\right\}\qquad(A\,5)$$

where a_e^u, a_w^u and a_n^v, a_s^v are the corresponding coefficients that come from the u and v momentum equations that are discretized in the east, west, north and south faces of the control volume for the pressure equation. Finally, the corrections for the velocities, u' and v', are computed with (Patankar 1980, pp. 124–126)

$$u'_e = d_e(p'_P - p'_E),\ u'_w = d_w(p'_W - p'_E),\ v'_n = d_n(p'_P - p'_N),\ v'_s = d_s(p'_S - p'_P). \quad \text{(A 6)}$$

Note also that this procedure is applied to both solid and fluid phases separately, and in the case of the solid-phase momentum equations (2.26), the inclusion of the solid pressure closure (2.19) implies that the pressure-correction equation is applied only at points where the flow is packed, that is, at points in which the flow is incompressible.

Finally, it is important to mention that for solving the convection-diffusion equation, two kinds of boundary conditions can be chosen: a given boundary value or a given boundary flux. As the momentum equations are a particular case of this general equation, the same boundary condition treatment applies to them as well. The only difference is that for the pressure-correction equation an additional condition at the boundary has to be given, which could be the pressure at the boundary (and the normal velocity is then unknown) or the normal velocity at the boundary (and the pressure is then unknown) (Patankar 1980, pp. 129–130).

REFERENCES

Ancey, C. 2007 Plasticity and geophysical flows: a review. *J. Non-Newtonian Fluid Mech.* **142**, 4–35.

Anderson, T. B. & Jackson, R. 1967 A fluid mechanical description of fluidized beds: equations of motion. *Ind. Engng Chem. Fundam.* **6**, 527–539.

Bagnold, R. A. 1954 Experiments on a gravity-free dispersion of large solid spheres in a Newtonian fluid under shear. *Proc. R. Soc. Lond. Ser.* A **225**, 49–63.

Balmforth, N. J. & Kerswell, R. R. 2005 Granular collapse in two dimensions. *J. Fluid Mech.* **538**, 399–428.

Bedford, A. 1983 Recent advances: theories of immiscible and structured mixtures. *Intl J. Engng Sci.* **21**, 863–960.

Boussinesq, J. 1877 Théorie de l'écoulement tourbillant. *Mem. Présentés par Divers Savants Acad. Sci. Inst. Fr.* **23**, 46–50.

Campbell, C. 1990 Rapid granular flows. *Annu. Rev. Fluid Mech.* **22**, 57–92.

Campbell, C. 2006 Granular material flows: an overview. *Powder Technol.* **162**, 208–229.

Cassar, C., Nicolas, M. & Pouliquen, O. 2005 Submarine granular flows down inclined planes. *Phys. Fluids* **17**, 103301.

Crowe, C. T. 2000 On models for turbulence modulation in fluid-particle flows. *Intl J. Multiphase Flow* **26**, 719–727.

Crowe, C. T., Troutt, R. & Chung, J. N. 1996 Numerical models for two-phase turbulent flows. *Annu. Rev. Fluid. Mech.* **28**, 11–43.

Dallavalle, J. M. 1948 *Micromeritics: The Technology of Fine Particles*, 2nd ed. Pitman.

Di Felice, R. 1994 The voidage function for fluid–particle interaction systems. *Intl J. Multiphase Flow* **20**, 153–159.

Di Felice, R. 1995 Hydrodynamics of liquid fluidisation. *Chem. Engng Sci.* **50**, 1213–1245.

Drew, D. A. 1983 Mathematical modelling of two-phase flow. *Annu. Rev. Fluid Mech.* **15**, 261–291.

Elghobashi, S. & Truesdell, G. C. 1993 On the two-way interaction between homogeneous turbulence and dispersed solid particles. II. Turbulence modification. *Phys. Fluids* **5**, 1790–1801.

Forterre, Y. & Pouliquen, O. 2008 Flows of dense granular media. *Annu. Rev. Fluid Mech.* **40**, 1–24.

Goldhirsch, I. 2003 Rapid granular flows. *Annu. Rev. Fluid Mech.* **35**, 267–293.

Goodman, M. & Cowin, S. 1971 Two problems in the gravity flow of granular materials. *J. Fluid Mech.* **45**, 321–339.

Hutter, K., Wang, Y. & Pudasaini, S. 2005 The Savage–Hutter avalanche model: how far can it be pushed? *Phil. Trans. R. Soc.* A **363**, 1507 – 1528.

Iverson, R. 1997 The physics of debris flows. *Rev. Geophys.* **35**, 245–296.

Iverson, R. & Denlinger, R. 2001 Flow of variably fluidized granular masses across three-dimensional terrain. 1. Coulomb mixture theory. *J. Geophys. Res.* **106**, 537–552.

Jackson, R. 2000 *The Dynamics of Fluidized Particles*. Cambridge University Press.

Jenkins, J. T. & Savage, S. B. 1983 A theory for the rapid flow of identical, smooth, nearly elastic, spherical particles. *J. Fluid Mech.* **130**, 187–202.

Johnson, P. C. & Jackson, R. 1987 Frictional–collisional constitutive relations for granular materials, with application to plane shearing. *J. Fluid Mech.* **176**, 67–93.

Joseph, D. & Lundgren, T. 1990 Ensemble averaged and mixture theory equations for incompressible fluid–particle suspensions. *Intl J. Multiphase Flow* **16**, 3542.

Kármán, T. von 1940 The engineer grapples with nonlinear problems. *Bull. Am. Math. Soc.* **46**, 615–683.

Lajeunesse, E., Monnier, J. & Homsy, G. 2005 Granular slumping on a horizontal surface. *Phys. Fluids* **17**, 103302.

Larrieu, E., Staron, L. & Hinch, E. 2006 Raining into shallow water as a description of the collapse of a column of grains. *J. Fluid Mech.* **554**, 259–270.

Lube, G., Huppert, H., Sparks, R. & Freundt, A. 2005 Collapses of two-dimensional granular columns. *Phys. Rev.* E **72**, 041301.

Lun, C. K. K., Savage, B. & Jeffrey, D. J. 1984 Kinetic theories for granular flow: inelastic particles in Couette flow and slightly inelastic particles in a general flow field. *J. Fluid Mech.* **140**, 223–256.

MiDi, GDR 2004 On dense granular flows. *Eur. Phys. J.* E **14**, 341–365.

Morland, L. W. 1992 Flow of viscous fluids through a porous deformable matrix. *Surv. Geophys.* **13**, 209–268.

Morland, L. & Sellers, S. 2001 Multiphase mixtures and singular surfaces. *Intl J. Non-Linear Mech.* **36**, 131–146.

Passman, S. L., Nunziato, J. W. & Walsh, E. K. 1984 *A Theory of Multiphase Mixtures*. Appendix 5C, Rational thermodynamics (ed. C. Truesdell), pp. 286–325. Springer.

Patankar, S.V. 1980 *Numerical Heat Transfer and Fluid Flow*. Hemisphere.

Pitman, B. & Le, L. 2005 A two-fluid model for avalanche and debris flows. *Phil. Trans. R. Soc.* A **363**, 1573–1601.

Pope, S. 2000 *Turbulent Flows*. Cambridge University Press.

Reynolds, O. 1895 On the dynamical theory of turbulent incompressible viscous fluids and the determination of the criterion. *Phil. Trans. R. Soc.* A **186**, 121–161.

Rodi, W. 1983 *Turbulence Models and Their Application in Hydraulics: A State-Of-The-Art Review*. IAHR.

Savage, S. B. 1983 Mechanical of granular materials: new models and constitutive relations. In *Granular Flows Down Rough Inclines: Review and Extension* (ed. J. T. Jenkins and M. Satake), pp. 261–282. Elsevier.

Staron, L. & Hinch, E. J. 2005 Study of the collapse of granular columns using two-dimensional discrete-grain simulation. *J. Fluid Mech.* **545**, 1–27.

Stewart, H. B. & Wendroff, B. 1984 Two-phase flow: models and methods. *J. Comput. Phys.* **56**, 363–409.

Sundaresan, S. 2003 Instabilities in fluidized beds. *Annu. Rev. Fluid Mech.* **35**, 63–88.

Truesdell, C. 1957 Sulle basi della thermomecanica. *Rand Lincei, Ser.* **8**, 33–38.

Truesdell, C. 1984 *Rational Thermodynamics*. Springer.

Wang, Y. & Hutter, K. 2001 Geomorphological fluid mechanics. In *Granular Material Theories Revisited* (ed. N. J. Balmforth and A. Provenzale), pp. 79–107. Springer.

Ystrom, J. 2001 On two-fluid equations for dispersed incompressible two-phase flow. *Comput. Visual. Sci.* **4**, 125–135.